

See discussions, stats, and author profiles for this publication at: <https://www.researchgate.net/publication/231647949>

An X-ray Absorption Spectroscopy Study of the Cathodic Discharge of $\text{Ag}_2\text{VO}_2\text{PO}_4$: Geometric and Electronic Structure Characterization of Intermediate phases and Mechanistic Insights

ARTICLE in THE JOURNAL OF PHYSICAL CHEMISTRY C · JULY 2011

Impact Factor: 4.77 · DOI: 10.1021/jp203924w

CITATIONS

20

READS

97

10 AUTHORS, INCLUDING:



Christopher Patridge

University at Buffalo, The State University of ...

19 PUBLICATIONS 262 CITATIONS

SEE PROFILE



Tesfaye Abtew

University at Buffalo, The State University of ...

38 PUBLICATIONS 303 CITATIONS

SEE PROFILE



Peihong Zhang

University at Buffalo, The State University of ...

92 PUBLICATIONS 1,637 CITATIONS

SEE PROFILE



Esther S. Takeuchi

Stony Brook University

109 PUBLICATIONS 1,334 CITATIONS

SEE PROFILE

An X-ray Absorption Spectroscopy Study of the Cathodic Discharge of $\text{Ag}_2\text{VO}_2\text{PO}_4$: Geometric and Electronic Structure Characterization of Intermediate phases and Mechanistic Insights

Christopher J. Patridge,[†] Chernojaye,[‡] Tesfaye A. Abtew,[§] Bruce Ravel,[‡] Daniel A. Fischer,[‡] Amy C. Marschilok,^{†,||,⊥} Peihong Zhang,[§] Kenneth J. Takeuchi,^{*,†} Esther S. Takeuchi,^{*,†,||,⊥,||} and Sarbajit Banerjee^{*,†}

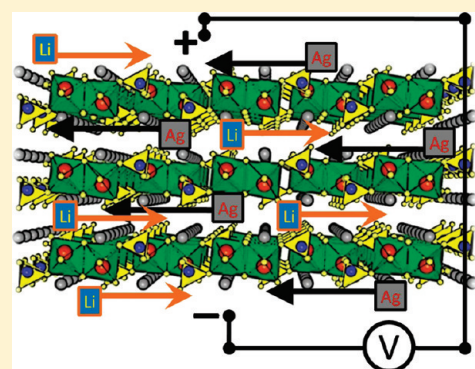
[†]Department of Chemistry, University at Buffalo, The State University of New York, Buffalo, New York 14260-3000, United States

[‡]Materials Measurement Laboratory, National Institute of Standards and Technology, Gaithersburg, Maryland 20899, United States

[§]Department of Physics, ^{||}Department of Electrical Engineering, [⊥]Department of Chemical and Biological Engineering, and

^{||}Department of Biomedical Engineering, University at Buffalo, The State University of New York, Buffalo, New York 14260, United States

ABSTRACT: Bimetallic phosphorus oxides have emerged as attractive candidates for use as cathode materials in the next generation of lithium-based batteries owing to the operation of multielectron transfer processes and thermochemical stabilities conferred by the incorporation of phosphate groups. In particular silver vanadium phosphorus oxide, $\text{Ag}_2\text{VO}_2\text{PO}_4$, shows a much desired in situ conductivity enhancement upon discharge resulting in inherently high power capability with minimal conductive additives needed. However, the amorphization of $\text{Ag}_2\text{VO}_2\text{PO}_4$ during electrochemical discharge precludes the use of standard diffraction tools to monitor changes in the local electronic and geometric structure. Here, we have utilized a combination of V K-, V L-, Ag K-, and O K-edge X-ray absorption fine structure spectroscopy to determine the local vanadium and silver oxidation states, local coordination geometry, and stoichiometry for $\text{Ag}_2\text{VO}_2\text{PO}_4$ samples with varying extents of electrochemical lithiation. Soft X-ray V L- and O K-edge measurements provide a detailed orbital-specific picture of changes in vanadium electronic structure upon discharge.



INTRODUCTION

Advances in electrochemical energy storage are critical to fully utilize hard-won gains in energy harvesting achieved via photovoltaics, thermoelectrics, and the better harnessing of renewable energy sources such as wind, hydroelectric, and geothermal power. The development of primary Li and rechargeable Li-ion batteries exhibiting high energy and power densities is at the heart of this puzzle and indeed also imperative to satisfy the increasing demand for energy for personal electronics.¹ Despite advances in the optimization of cathode materials over the last several decades,² there remains an urgent need to enhance cathodic utilization efficiencies and to develop materials that can safely deliver high power and energy densities continuously over hundreds of cycles. Two broad strategies have been adopted to address this challenge: (a) the design and preparation of compositionally new cathode materials with specific structural characteristics that enable rapid and facile Li-ion insertion/extraction and provide a high specific charge and charge density;³ and (b) tuning the properties of known electrode materials by scaling to nanoscale dimensions, controllably introducing defects, or modifying the surfaces to incorporate highly mobile or conducting phases.^{2d,4}

Materials discovery for utilization of cathode materials has been substantially rethought with the realization that classical intercalation chemistry within layered compounds is not a prerequisite for thermodynamically and kinetically feasible Li-ion insertion/extraction reactions.^{2a,4b,4d} A number of design principles have started to emerge that allow rational control of phase stabilities, potential windows, cycling efficiencies, and reaction kinetics based on optimization of specific structural characteristics and tunability of interfacial and surface properties of composite electrode materials. Consequently, one of the most vexingly demanding requirements for a cathode material, the need to simultaneously maintain optimal electronic and ionic transport, has considerably been addressed by the controlled incorporation of surface coatings, precise selection of stoichiometry, or the incorporation of dopant phases.^{2d,4,5} However, tuning the material composition and structure appropriately to create a conductive material on discharge is desirable, as this

Received: April 28, 2011

Revised: June 7, 2011

Published: July 06, 2011

precludes the need for surface coating or other post processing methods.

Some particularly noteworthy examples of structure design to ensure retention of ionic and electronic transport up to deep discharge include layered vanadium oxide structures.⁶ Silver vanadium oxide ($\text{Ag}_2\text{V}_4\text{O}_{11}$) has gained particular notoriety as the cathode material that enabled development of the implantable cardiac defibrillator battery and remains the dominant technology.⁷ The discharge of silver vanadium oxide progresses with the reduction of Ag^+ to Ag^0 and reduction of the vanadium centers from V^{5+} to V^{4+} and V^{3+} .⁸ The reduced silver ions form metallic silver particles and nanowires on the surface of the active material particles. Consistent with the formation of the silver metal matrix, the cathode conductivity increases with discharge. Copper vanadium oxides have also been investigated for their use as cathode materials in lithium-based systems.⁹ A series of copper bronzes with nominal compositions $\text{Cu}_{2.33}\text{V}_4\text{O}_{11}$ and $\text{Cu}_{1.1}\text{V}_4\text{O}_{11}$ has been prepared that exhibit stable capacities of 250 and 260 mAh/g, respectively.¹⁰ These materials undergo a reversible Li-driven displacement process featuring the cyclic formation and disappearance of Cu dendrites.^{10b} All of the aforementioned materials have structures based upon layers of V_4O_{11} units and despite not being classical intercalation hosts undergo an unusual and remarkable electrochemical reaction with Li ions involving a displacement process featuring the formation of metal nanoparticles, accompanied by the amorphization of the parent electrode material.^{10b}

Recent research attention has focused on phosphate derivatives of silver vanadate phases inspired by the greater chemical stability of PO_4^{3-} moieties. The $\text{M}_{\text{TM}}\text{—O—P}$ coupling of strong covalent phosphate tetrahedra confers thermal and chemical stability to a variety of crystal structures. From a crystal field perspective, the inductive effects of phosphorus are electronically reflected in increased antibonding character and reduced covalency of M—O linkages, which thereby produces an increase in the transition metal potentials. These effects have most notably been evidenced in a number of transition metal phosphorus oxides including the well-studied olivine structure LiMPO_4 ($\text{M} = \text{Fe}, \text{Ni}, \text{and Mn}$), which exhibits good capacity at moderate rates of 5C.¹¹ Bimetallic analogues of these materials are particularly attractive due to the demonstrated realization of multiple electron transfer.¹²

Recent work by some of the authors of this submission demonstrates that the amorphization of $\text{Ag}_2\text{VO}_2\text{PO}_4$ upon Li-ion insertion is accompanied by the formation of Ag nanoparticles; the latter form a conductive metallic matrix that enhances the electrical conductivity of the in situ generated composite of $\text{Li}_x\text{Ag}_{2-x}\text{VO}_2\text{PO}_4$ and metallic Ag nanoparticles by 15 000 fold relative to the parent $\text{Ag}_2\text{VO}_2\text{PO}_4$ material.^{12b} The in situ generation of a conductive matrix ensures intimate electrical contact for a majority of the electrode material and avoids many processing problems that arise by using composite/coated materials such as the localization of electrochemical reactions only to regions characterized by the ternary confluence of the electrolyte, the cathode material, and the conductive additive. Consistent with this discharge mechanism, $\text{Ag}_2\text{VO}_2\text{PO}_4$ material with smaller crystallite size, smaller particle size, and higher surface area showed improved power capability under constant current and pulse conditions due to a uniform dispersion of silver nanoparticles throughout the cathode matrix.¹³ However, the concomitant amorphization of the host vanadium phosphorus oxide matrix renders it difficult to monitor structural changes

upon lithiation using conventional diffraction tools.^{12b} Magnetic susceptibility of partially reduced $\text{Ag}_2\text{VO}_2\text{PO}_4$ samples has been previously used to gain information regarding the progression of the oxidation state of the vanadium centers with discharge.¹⁴ The collected data revealed a regular increase in magnetic susceptibility upon reduction, consistent with progression from $\text{V}^{5+} \rightarrow \text{V}^{4+} \rightarrow \text{V}^{3+}$ and d electron configuration changes of $d^0 \rightarrow d^1 \rightarrow d^2$. However, there remains a paucity of information pertaining to changes in the local vanadium and silver coordination environments of $\text{Ag}_2\text{VO}_2\text{PO}_4$ upon lithiation thus representing a critical gap in our knowledge of this system which needs to be addressed to enable rational materials design and optimization.

We present here a comprehensive X-ray absorption fine structure (XAFS) spectroscopy study aimed at elucidating alterations in local and intermediate geometric structure as well as the electronic structure of $\text{Ag}_2\text{VO}_2\text{PO}_4$ upon Li-ion insertion within the active electrode material. As an element-specific probe, XAFS presents no crystallinity requirements and can be applied to most elements in the periodic table.¹⁵ In this submission, we use a combination of X-ray absorption near edge structure (XANES) measurements at V L-, O K-, V K-, and Ag K-edges in conjunction with extended X-ray absorption fine structure (EXAFS) measurements at the Ag K-edge to extract a fairly detailed mechanistic picture of structural transformations manifested in the $\text{Ag}_2\text{VO}_2\text{PO}_4$ host material upon electrochemical lithiation. We also present the first band structure calculations of $\text{Ag}_2\text{VO}_2\text{PO}_4$ and use this set of data to obtain a more detailed understanding of the electronic structure of this material.

■ EXPERIMENTAL SECTION

Synthesis of $\text{Ag}_2\text{VO}_2\text{PO}_4$. $\text{Ag}_2\text{VO}_2\text{PO}_4$ was synthesized by a facile hydrothermal process described previously in the literature.^{12b,16} Briefly, $\text{Ag}_2\text{VO}_2\text{PO}_4$ was hydrothermally prepared from Ag_2O , V_2O_5 , and H_3PO_4 precursors in aqueous solution by heating a mixture of the precursors at 230 °C in a Teflon-lined autoclave for 96 h. The powder was collected using vacuum filtration and subsequently dried under vacuum.

Cathode and Coin Cell Fabrication. Coin cells were fabricated within an argon-filled glovebox. The discharged materials examined here were prepared using pure, as-synthesized $\text{Ag}_2\text{VO}_2\text{PO}_4$ material sans binder. One M LiAsF₆ in 50/50 (v/v) propylene carbonate/dimethoxyethane were used as the electrolyte component in all the coin cells. A lithium metal foil was deployed as the anode. Each coin cell was discharged using a C/200 rate at 37 °C. The discharge reaction was halted at various depths of discharge and the requisite cells were allowed to recover at open circuit potential. The cathode material with varying extents of electrochemical reduction^{12b} was recovered from the coin cells and was placed within double layers of Kapton tape after ball milling with an inert BN matrix using a Spex 5100 Mixer Mill for hard X-ray XANES and EXAFS experiments. Soft X-ray NEXAFS experiments were performed on the as-recovered powders pressed onto Cu tape. Five samples, corresponding to various extents of lithiation, denoted as 0, 25, 50, 75, and 100% depth of discharge were analyzed in this study. The 0% sample DOD sample represents the $\text{Ag}_2\text{VO}_2\text{PO}_4$ powder assembled within a cell and then recovered without any electrochemical testing.

Morphological and Elemental Analysis. Scanning electron microscopy (SEM) data were collected using a Hitachi SU-70

field-emission scanning electron microscope equipped with an Oxford Inca energy-dispersive X-ray spectroscopy (EDS) system. Backscattered electron microscopy images were obtained and EDS spectra were collected at an accelerating voltage of 20 kV.

X-ray Absorption Spectroscopy. XAFS measurements of recovered cathode samples with varying extents of lithiation were acquired at the vanadium L- and oxygen K-edges at the National Institute of Standards and Technology (NIST) beamline U7A at the National Synchrotron Light Source (NSLS) of Brookhaven National Laboratory. A toroidal mirror spherical grating monochromator was used for these measurements, yielding a spectral resolution of ~ 0.1 eV. All spectra were acquired in partial electron yield (PEY) mode using a channeltron electron multiplier detector located near the sample. An entrance grid bias of -150 V was used for all spectra presented here. A charge compensation gun was used to avoid sample charging since the samples exhibit varying electrical conductivities. A metallic vanadium mesh was used as a reference standard for calibration of the energy scale for V L- and O K-edge spectra. To eliminate the effects of monochromator absorption features and incident beam intensity fluctuations, the PEY signals were normalized using the drain current of a freshly evaporated gold mesh with 90% transmittance located along the path of the incident X-rays. Spectra were acquired at magic angle (54.7°) incidence of the X-ray beam to eliminate preferential orientation effects. Pre- and postedge normalization of spectra were performed using Athena¹⁷ to obtain an edge jump of unity for all the samples, enabling normalization across different absorption cross sections.

V K- and Ag K-edge XAFS spectra were measured in transmission mode at NIST beamline X23A2 of the NSLS for powdered samples of the discharged cathode material diluted with BN. A Si(311) monochromator was used with an overall spectral resolution ($\Delta E/E$) of 2×10^{-4} . Ionization chambers were used to detect the incident and transmitted flux. Data were processed using ATHENA with the AUTOBK background removal algorithm.^{17,18} The spectra were pre- and postedge normalized to again obtain an edge jump of unity to facilitate comparisons across different samples. All spectra were calibrated and aligned using vanadium and silver metal foil standards data collected simultaneously at their respective edges using a third ionization chamber. In addition, spectral data were acquired for an extensive array of vanadium oxide standards to enable development of XANES calibration plots. EXAFS modeling was carried out using the IFFEFIT suite of programs.^{17,18} FEFF6 calculations were used to determine all scattering paths in a cluster of ~ 40 atoms out to a distance of 5 Å from the photoabsorbing atom using single crystal data for $\text{Ag}_2\text{VO}_2\text{PO}_4$ obtained from the Cambridge Crystallographic Data Center (Joint Committee of Powder Diffraction Standards (JCPDS # 01-081-2149)).¹⁶ The k -range was set from 2 – 10 Å⁻¹ and the Fourier transform (FT) ranges were fit between 1.1 – 3.8 Å for Ag K-edge data using Hanning windows ($dk = 0.5$). ARTEMIS parameters E_0 and R_{bkg} were consistently fixed at 25.52 keV and 1.15, respectively, for all the data sets analyzed at the Ag K-edge. The EXAFS fitting contains the scattering amplitude parameter Amp, the Debye–Waller factor σ^2 , and the energy shift ΔE_0 . A single scattering path shift ΔR was used making for a total of four fitting parameter for all paths. The modeled data for $\text{Ag}_2\text{VO}_2\text{PO}_4$ excluded paths indicated as being insignificant by FEFF6 within the specified fitting range. Multiple silver standards were used to establish the

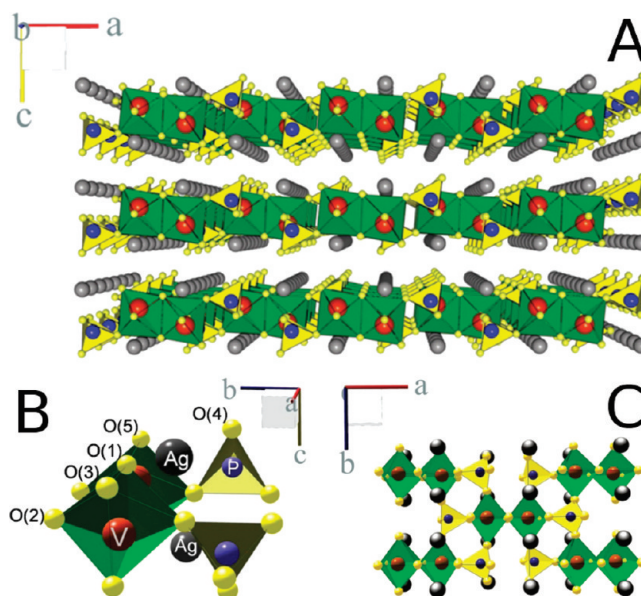


Figure 1. (A) Crystal structure of $\text{Ag}_2\text{VO}_2\text{PO}_4$; green $[\text{VO}_6]$ octahedra are seen enclosing vanadium atoms depicted in red; yellow PO_4^{3-} tetrahedra enclose phosphorus atoms depicted in blue; Ag (gray spheres) reside between VPO_6 layers in the ab plane aligning along the b -axis. (B) Perspective view of the $\text{Ag}_2\text{VO}_2\text{PO}_4$ crystal structure along the crystallographic a -axis indicating the five unique oxygen positions. (C) Perspective view along the crystallographic c -axis showing the ab -plane with each PO_4^{3-} tetrahedron connecting three double $[\text{VO}_6]$ polyhedra.

absorber attenuation factor S_0^2 , yielding a value of 0.84 for silver atoms. Additionally the refined structural coordination number was constrained during fitting allowing for additional parameters x and y to calculate relative percentage compositions. Linear combination fitting (LCF) was performed in ATHENA using spectra for the two crystalline end members, $\text{Ag}_2\text{VO}_2\text{PO}_4$ and Ag metal, as the absorption standards.

Theoretical Calculations. Density functional theory (DFT) as implemented in the Quantum ESPRESSO package was used to determine the atom- and orbital-projected density of states for $\text{Ag}_2\text{VO}_2\text{PO}_4$ from first-principles considerations.¹⁹ The generalized gradient approximation²⁰ was used for exchange and correlation terms along with ultrasoft pseudopotentials²¹ to describe the electron-ion interactions. The starting structure was taken from crystallographic data reported by Kang et al.¹⁶

RESULTS AND DISCUSSION

Structural Details. $\text{Ag}_2\text{VO}_2\text{PO}_4$ crystallizes in the $C2/m$ monoclinic space group with distorted edge-linked $[\text{VO}_6]$ octahedra and $[\text{PO}_4]$ tetrahedra arrayed parallel to the (001) plane with Ag^+ ions residing between the layers, as depicted in Figure 1A.¹⁶ Figure 1B illustrates the five crystallographically inequivalent oxygen atoms of this structure with two short, two intermediate, and two long V–O bonds. A pair of $[\text{VO}_6]$ octahedra share a common edge to constitute dimers with overall V–V separation of ~ 3.1 Å. Each $[\text{PO}_4]$ tetrahedron shares corners with three adjacent edge-linked $[\text{VO}_6]$ – $[\text{VO}_6]$ dimer pairs with only one of the oxygen atoms of the phosphate group directly oriented toward the interlayer region where the octahedrally coordinated Ag^+ ions reside. Apart from the open layers

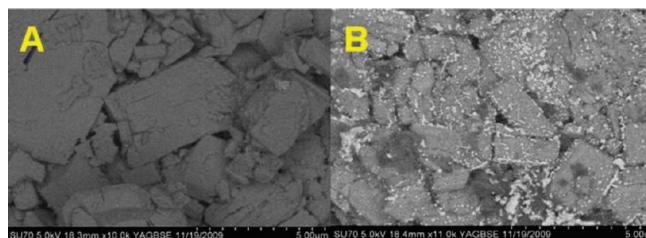


Figure 2. Scanning electron microscopy backscattered images: (A) 0% DOD, (B) 50% DOD; image A suggests a homogeneous elemental makeup, whereas image B is characterized by regions of high contrast attributed to metallic Ag nanoclusters. EDX confirms disproportionate Ag content within the high-contrast areas.

in the *ab* plane, two distinctive channels can be visualized along the crystallographic *c*-axis, as shown in Figure 1C, defined by alternating edges of $[\text{VO}_6]$ octahedra and $[\text{PO}_4]$ tetrahedra.¹⁶ The Ag ions can be perceived as residing along the sidewalls of these channels (with considerable disorder in their occupancies), which also clearly illustrates the open spaces available in this framework for Li-ion intercalation.

The XAFS probes used here are particularly sensitive to changes in the local electronic and geometric structure of vanadium. As highlighted in Figure 1B, the V^{5+} ion resides within a distorted octahedral environment with two oxygen atoms located in close proximity ($\text{V}-\text{O}(1)$ bond length of 1.689 Å; $\text{V}-\text{O}(5)$ bond length of 1.620 Å) and oriented in a *cis* configuration relative to each other. Additionally, two equivalent oxygen atoms ($\text{O}(2)$) are at a distance of 1.958 Å, and the octahedron is completed by two long $\text{V}-\text{O}$ bonds ($\text{V}-\text{O}(3)$ at 2.139 Å and $\text{V}-\text{O}(1')$ at 2.318 Å). The local bonding environment of the phosphorus atom has a distinctive oxygen atom (denoted as $\text{O}(4)$ in Figure 1B), uninvolved in edge sharing with $[\text{VO}_6]$ octahedra, coordinated exclusively to Ag^+ ions with bond distances ranging from 2.2–2.7 Å.

Electrochemical Lithiation and Electron Microscopy. As a demonstrated multielectron transfer material, the discharge process for $\text{Ag}_2\text{VO}_2\text{PO}_4$ is expected to be accompanied by discrete redox reactions at the two transition metal centers



and



12,14

Extensive electrochemical testing indicates the realization of near theoretical capacity (270 mAh/g) at 1.5 V with a volumetric capacity of 1440 mAh/cm³ derived from the four-electron transfer redox reactions noted in eqs 1 and 2.^{12,14} The precedence of Ag^+ reduction, at least upon initiation of discharge, has also been demonstrated by the 15 000 fold drop in electrical resistivity and the formation of Ag nanoparticles, which presumably achieve percolation.^{12b}

Figure 2 shows elemental-composition-sensitive backscattered electron SEM images of $\text{Ag}_2\text{VO}_2\text{PO}_4$ samples with 0 and 50% depth of discharge. The appearance of bright intensely scattering Ag nanoparticles is clearly discernible in Figure 2B, reflecting the higher average atomic number of the Ag metallic phases relative to the vanadium phosphorus oxide matrix. Quantitative EDS studies further indicate disproportionate Ag composition

localized within the brighter regions, further corroborating the formation of metallic Ag nanoparticles. Metallic Ag formation in partially discharged $\text{Ag}_2\text{VO}_2\text{PO}_4$ was confirmed by X-ray powder diffraction analysis in previous work, where Ag^0 formation was found to initiate at the onset of electrochemical reduction.^{12b}

X-ray Absorption Fine Structure (XAFS) Spectroscopy.

While detection of Ag^0 was possible using X-ray powder diffraction of electrochemically reduced $\text{Ag}_2\text{VO}_2\text{PO}_4$, the amorphization of the parent $\text{Ag}_2\text{VO}_2\text{PO}_4$ material limits the utility of conventional powder diffraction to determine structural evolution of the $\text{V}-\text{O}-\text{P}-\text{O}$ framework. Element-specific X-ray absorption spectroscopy techniques have been deployed to elucidate changes in the local geometric and electronic structure induced upon electrochemical lithiation. The X-ray absorption probability for an individual photoabsorber atom in a material is modulated by its chemical environment and thus the spectral features (depending on the atom and specific absorption edge) are reflective of the formal oxidation state, coordination number, species of surrounding atoms, the alignment of specific bonds within a structure, and the electronic structure of the material.^{15,22} Spectral features ranging to about 40–50 eV above the edge are denoted as near-edge X-ray absorption fine structure (NEXAFS) or XANES features, whereas features 50–1000 eV above the edge constitute the extended X-ray absorption fine structure (EXAFS) spectrum of the material. Here, we have combined XANES data acquired at V L-, O K-, V K-, and Ag K-edges with EXAFS data measured at the Ag K-edge to develop a detailed picture of changes in the Ag and V local coordination environments upon discharge. XANES and EXAFS investigations at the V K-edge have proved to be exceedingly informative in elucidation of the local coordination environments and structural identification of phases with intermediate degrees of lithiation for V_6O_{13} and $\text{Ag}_2\text{V}_4\text{O}_{11}$ parent electrode materials.²³ Soft X-ray V L- and O K-edge NEXAFS spectroscopy studies have also provided valuable insight into the electronic structure (especially the unoccupied density of states (UDOS)) and nature of chemical bonding in various binary vanadium oxide and vanadium oxyphosphate phases.²⁴

V K-Edge. In light of the electric dipole selection rules operational for XANES spectroscopy (change in angular momentum $\Delta l = \pm 1$ and spin-flips being forbidden, $\Delta j = 0, \pm 1$),^{22b,25} a finite transition probability at the V K-edge reflects transitions from the 1s core levels of vanadium to the p components of V 3d–ligand 2p hybridized states.^{25,26} The features at this edge thus contain a wealth of information regarding energy band dispersion effects, the local coordination environment, and the nature of V–ligand bonding, reflecting the relatively delocalized nature of the final states.²⁷ In contrast, the V L-edges discussed below reflect transitions from V 2p \rightarrow V 3d states that are more atomic in character and thus yield more localized information about electronic structure.^{24c}

Figure 3A shows V K-edge XANES spectra acquired for $\text{Ag}_2\text{VO}_2\text{PO}_4$ samples subjected to varying degrees of electrochemical lithiation. Each sample is individually denoted by the percentage depth of discharge. The V K-edge is characterized by an absorption onset (the threshold), followed by a prominent pre-edge feature (highlighted in Figure 3A), and an intense band corresponding to 1s \rightarrow 4p transitions, with the absorption edge appearing as a shoulder to the latter peak.^{26–28} As noted above, the pre-edge feature reflects electric-dipole-allowed transitions from 1s core levels to the p components of p–d hybridized states and thus the peak position, lineshapes, and intensities of this

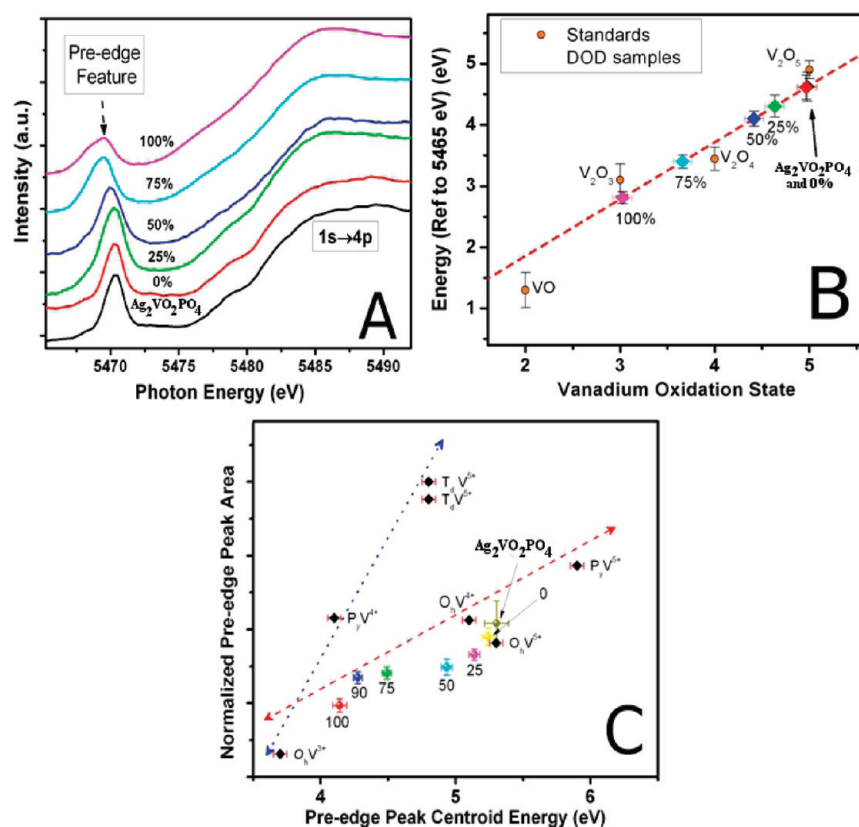


Figure 3. (A) Stacked plot of the near-edge absorption data at the vanadium K-edge region measured for $\text{Ag}_2\text{VO}_2\text{PO}_4$ samples with varying extents of electrochemical lithiation. (B) A pseudo-Voigt function has been fit to the pre-edge resonances of various vanadium oxide standards to construct a calibration curve exhibiting good linear correlation ($R > 0.98$). The calibration curve is used to determine the formal vanadium oxidation states for the test samples with varying extents of electrochemical lithiation. (C) A series of vanadium standards were used to develop a plot of peak intensity, peak position, and oxidation state; data for the following have been used to construct this 2D Chaurand plot with the local coordination geometries and oxidation states indicated within parentheses: NH_4VO_3 , NaVO_3 (T_dV^{5+}), V_2O_5 (P_jV^{5+}), V_2O_4 (O_hV^{4+}), V_2O_3 , VCl_3 (O_hV^{3+}).⁴² The lines are guides to the eye. The test samples have further been located within this 2D plot.

resonance serve as sensitive indicators of the extent of covalency, local coordination geometry, site symmetry, and the formal vanadium oxidation state.^{25,26,28}

The pre-edge resonance of vanadium oxides is derived primarily from strong V 3d–O 2p hybridization, which imparts significant ungerade p character to the relevant unoccupied density of states, enabling a finite transition probability. In this context, the binary vanadium oxide VO crystallizes with perfectly octahedral symmetry in the rock salt structure, geometrically precluding substantial p–d hybridization; consequently, no discernible pre-edge resonance is observed for this material.^{26,29} With increasing departure from octahedral symmetry, such as with Jahn–Teller distorted tetragonal VO_2 or square pyramidal V_2O_5 , stronger V 3d–O 2p hybridization is obtained and a more distinctive pre-edge resonance is discernible. Notably, a small but finite contribution to the pre-edge peak also originates from dipole-disallowed quadrupolar transitions.²⁷

The pronounced pre-edge peak noted for $\text{Ag}_2\text{VO}_2\text{PO}_4$ in Figure 3A reflects the considerable distortion from octahedral symmetry of the constituent edge-sharing $[\text{VO}_6]$ polyhedra, as clearly illustrated in Figure 1B. With increasing extent of lithiation, a clear broadening of the pre-edge feature and a shift to lower energies is apparent from the spectra shown in Figure 3A. The peak position of the pre-edge feature is closely correlated to the formal vanadium oxidation state according to Kunzl's law;

greater energy is required to promote a core electron for higher oxidation states due to the increased effective nuclear charge and reduced repulsion of electrons.^{26,28} The shift of peak maxima to lower energies observed in the experimental data thus implies reduction of V^{5+} centers in $\text{Ag}_2\text{VO}_2\text{PO}_4$.

To obtain a more quantitative understanding of the formal vanadium oxidation state as a function of the depth of discharge, the pre-edge feature for each sample has been fitted using a pseudo-Voigt function to account for core–hole lifetime and instrumental broadening effects. A systematic background function has been interpolated using several data points on both sides of the spectral feature. Such a fitting procedure allows direct extraction of area-weighted centroid values along with determination of experimental uncertainties. The centroid values are more reflective of broader lineshapes and are used in lieu of the energies of peak maxima.²⁸ Figure 3B plots a calibration curve for pre-edge centroid values of known binary vanadium oxide standards with different oxidation states, clearly indicating a linear and well-behaved correlation between the oxidation state and the experimentally determined energies of the XANES resonance. The peak positions of $\text{Ag}_2\text{VO}_2\text{PO}_4$ samples with varying extents of lithiation have been located within this plot and provide a good estimate of the nominal vanadium oxidation states. The 0% discharge and as-prepared $\text{Ag}_2\text{VO}_2\text{PO}_4$ samples exhibit the pre-edge resonance at approximately the same energy

Table 1. Calculated Oxidation States for the Series of Discharged Samples^a

depth of discharge	oxidation state	error \pm
0%	4.91	± 0.15
25%	4.64	± 0.18
50%	4.21	± 0.16
75%	3.53	± 0.13
100%	3.24	± 0.12

^a The error values derive from errors associated with fitting the pre-edge resonance peak using the pseudo-Voigt function.

within limits of error, suggesting that construction of the cell and mixing with the electrolyte does not substantially alter the vanadium coordination environment.

Table 1 tabulates the formal vanadium oxidation states deduced using the calibration curve from Figure 3B. Surprisingly, an oxidation state of 4.64 ± 0.18 , suggesting that 40% of all V^{5+} sites have been reduced to V^{4+} , is deduced for the sample at 25% depth of discharge, suggesting that Ag^+ and V^{5+} reduction are initiated concurrently and that the redox reactions noted in eqs 1 and 2 are not entirely sequential, perhaps as a result of kinetically influenced Li-ion insertion at $Ag_2VO_2PO_4$ particle surfaces. The marked broadening of the pre-edge lineshapes evidenced in Figure 3A is further suggestive of the existence of mixed valences of vanadium ions in the incipient amorphous lithiated phase. These results are consistent with the previously reported magnetic susceptibility findings where a regular increase in the magnetic susceptibility values was observed with progression of $Ag_2VO_2PO_4$ reduction indicating reduction of Ag^+ concurrently with V^{5+} .¹⁴ The results further parallel previous observations for $Ag_2V_4O_{11}$.^{23b}

Analogously, a formal oxidation state of 4.21 ± 0.16 is inferred for the sample discharged to 50%, suggesting some V^{5+} reduction but primarily Ag^+ reduction between 25 and 50% discharge. In contrast, a substantial decrease in the formal oxidation state is noted for the sample discharged to 75% (formal oxidation state of 3.53 ± 0.13), suggestive of increased vanadium reduction once the electrochemically accessible Ag^+ ions have been reduced to form Ag nanoparticles. At 100% discharge, the nominal value of 3.24 ± 0.12 shows further reduction of vanadium. Note that this provides a conservative estimate of vanadium reduction since if V^{5+} sites are still remnant in the material, a far greater extent of reduction down to V^{3+} would be required to maintain electro-neutrality. In principle, the completion of the redox reactions depicted in eqs 1 and 2 should yield the transfer of four electrons and an eventual vanadium oxidation state of +3. The slightly higher oxidation state measured here is likely due to the presence of remnant electrochemically inaccessible vanadium sites.

As noted above, the normalized intensity of the pre-edge resonance is strongly correlated to the local vanadium symmetry and the extent of p–d hybridization.^{25,28} Chaurand et al. have developed a methodology to simultaneously ascertain the local coordination geometry and the formal vanadium valence based on construction of a 2D plot of the normalized pre-edge intensity versus the peak position for various standards with known coordination geometries (octahedral, square pyramidal, and tetrahedral) and oxidation states (ranging from +2 to +5).²⁸ In Figure 3C, we have constructed an analogous plot based on data for different standards clearly delineating the locations of different coordination-geometry–oxidation-state combinations. The

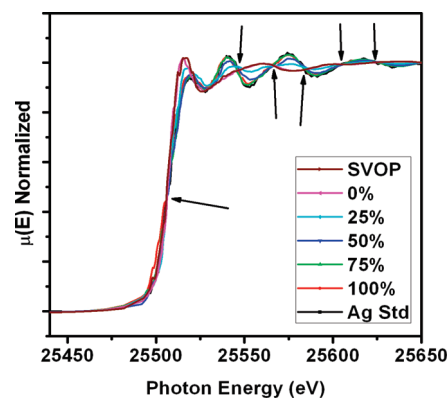


Figure 4. Ag K-edge near-edge region for $Ag_2VO_2PO_4$ samples with varying extents of electrochemical lithiation. The black arrows points to multiple isosbestic points throughout the region supporting direct $Ag^{1+} \rightarrow fcc\ Ag^0$ transformations and the existence of a two-phase system. Additional broadening is present at the edge jump suggestive of the presence of multiple Ag species (Ag^{1+} , Ag^0).

experimentally measured normalized intensities and peak positions of the pre-edge resonance for the $Ag_2VO_2PO_4$ samples with varying extents of discharge have also been mapped onto this plot, and again indicate a monotonic decrease in the oxidation state with increasing lithiation. Some reduction of V^{5+} sites in $Ag_2VO_2PO_4$ is noted even for 25% depth of discharge although it is clear from Figure 3C that vanadium reduction occurs predominantly between 50 and 100% depth of discharge. Interestingly, the intensity of the pre-edge peak suggests a strongly distorted octahedral coordination environment for vanadium in $Ag_2VO_2PO_4$ and retention of an octahedral, albeit distorted octahedral, geometry upon 100% discharge.

The low density of relatively light vanadium atoms surrounded by a preponderance of high atomic number Ag atoms gives rise to a strong scattering background and causes severe attenuation of the appropriate vanadium absorption lengths, making it difficult to acquire high-quality V K-edge absorption data at values significantly above the absorption edge, as required for EXAFS analysis. However, we have been able to acquire both XANES and EXAFS data at the Ag K-edge, which enables further insight into the structure of the amorphized lithiated phases.

Ag K-Edge. Figure 4 shows Ag K-edge XANES spectra acquired for $Ag_2VO_2PO_4$ and discharged samples with varying extents of electrochemical lithiation compared to data for a metallic Ag powder standard. The most striking feature of this data is the existence of five discrete isosbestic points (indicated by arrows in Figure 4), suggesting the stoichiometrically linear transformation of Ag^+ ions in $Ag_2VO_2PO_4$ to metallic Ag^0 in the Ag nanoparticles depicted in Figure 2B without stabilization of any detectable intermediate Ag-containing phases. In other words, during the discharge process, the Ag^+ ions reside along the walls of the channels of $Ag_2VO_2PO_4$ (as depicted in Figure 1C), octahedrally coordinated by oxygen atoms, or instead are ensconced within a face-centered cubic Ag^0 lattice. A similar stoichiometrically linear reduction of Ag^+ ions to form Ag nanoparticles was noted upon the lithiation of $Ag_2V_4O_{11}$.^{8,23b}

Closer inspection of the Ag K-edge resonances at 25.52 keV in Figure 4 show appreciable peak broadening consistent with contributions to the absorption edge data from multiple species (Ag^0 , Ag^+). We have further performed linear combination fitting (LCF) of the XANES data to quantitatively estimate the relative

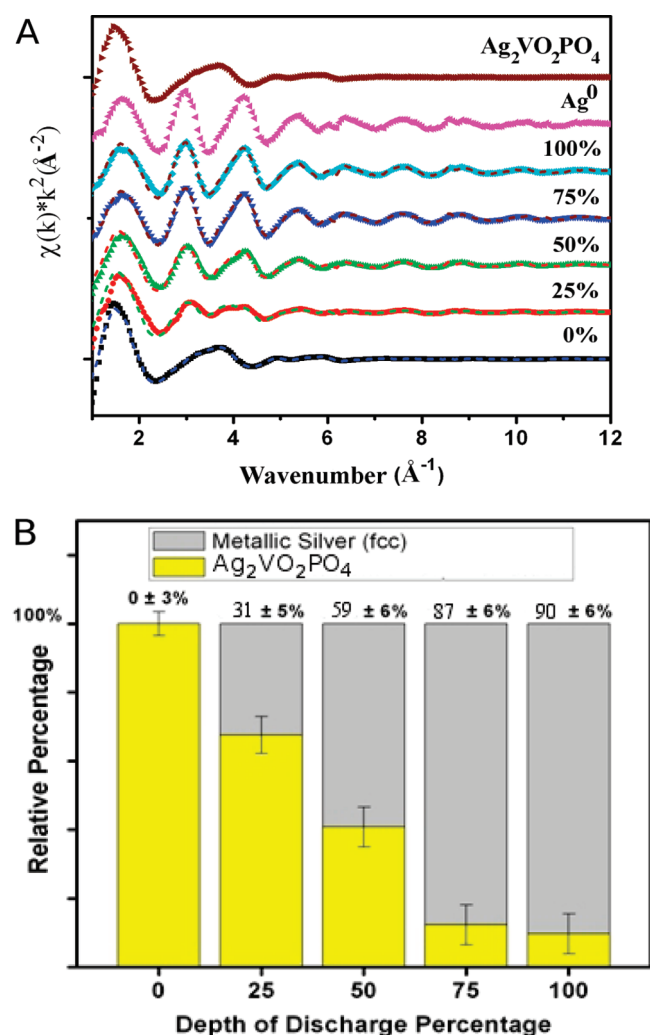


Figure 5. (A) Stack plots in k -space of end members $\text{Ag}_2\text{VO}_2\text{PO}_4$ and fcc Ag along with the five $\text{Ag}_2\text{VO}_2\text{PO}_4$ samples with varying depths of discharge. LCF was performed on each sample using the two standards to extract relative percentages of the two end members present at intermediate stages of the electrochemical lithiation/discharge process. (B) Each column represents a discharged sample with the two colors yellow representing Ag within a $\text{Ag}_2\text{VO}_2\text{PO}_4$ environment, and gray representing Ag in a fcc Ag environment. The included error bars are estimated from the uncertainty values in the implementation of the LCF method in Athena.

contributions from Ag^0 (metallic Ag) and Ag^+ ($\text{Ag}_2\text{VO}_2\text{PO}_4$) species. The stoichiometrically linear transformation of Ag-species between these two end phases makes LCF a reasonably accurate measure of the relative proportions of metallic Ag and remnant $\text{Ag}_2\text{VO}_2\text{PO}_4$. The Ag K-edge data for the varying extents of electrochemical lithiation have been transformed to reciprocal k -space (\AA^{-1}). Subsequently, we have used the data for Ag powder and as-prepared $\text{Ag}_2\text{VO}_2\text{PO}_4$ as standards to perform a LCF fit for each data set.

Figure 5B shows the relative percentages of the two local Ag coordination environments as a function of the extent of electrochemical lithiation. At 0% depth of discharge, all the Ag in the sample is present as $\text{Ag}_2\text{VO}_2\text{PO}_4$ and no metallic Ag is required to fit the data (Figure 5B). During the initial two discharge steps, the contributions from fcc metallic Ag have been

Table 2. Complete Cathode Compositions Using Values Extracted from V K- and Ag K-Edge Absorption Data^a

Nominal Chemical Compositions of the Material at Varying Depths of Discharge	
0%	$0 \text{ Ag}^0 + \text{Ag}_{1.40}^{(1+)}\text{V}_{1.00}^{(5+)}\text{O}_2\text{PO}_4$
25%	$0.60 \text{ Ag}^0 + \text{Ag}_{1.40}^{(1+)}\text{Li}_{1.00}^{(1+)}\text{V}_{0.40}^{(4+)}\text{V}_{0.60}^{(5+)}\text{O}_2\text{PO}_4$
50%	$1.25 \text{ Ag}^0 + \text{Ag}_{0.8}^{(1+)}\text{Li}_{1.95}^{(1+)}\text{V}_{0.75}^{(4+)}\text{V}_{0.25}^{(5+)}\text{O}_2\text{PO}_4$
75%	$1.72 \text{ Ag}^0 + \text{Ag}_{0.28}^{(1+)}\text{Li}_{3.2}^{(1+)}\text{V}_{0.50}^{(3+)}\text{V}_{0.50}^{(4+)}\text{O}_2\text{PO}_4$
100%	$1.90 \text{ Ag}^0 + \text{Ag}_{0.10}^{(1+)}\text{Li}_{3.7}^{(1+)}\text{V}_{0.80}^{(3+)}\text{V}_{0.20}^{(4+)}\text{O}_2\text{PO}_4$

^aThe caveat in assigning oxidation states of vanadium, it was assumed at 75% and beyond, the main composition should consist of V^{3+} and V^{4+} . Vanadium stoichiometry uncertainties are estimated at ± 0.088 and Ag uncertainties are estimated at ± 0.042 .

determined to be $31 \pm 5\%$ at 25% DOD and $59 \pm 6\%$ at 50% DOD, which indicates somewhat higher metallic Ag formation than previously determined from powder XRD measurements. XANES techniques are likely more accurate for quantification of Ag coordination environments given the high sensitivity to the local coordination environment of the photoabsorber and the clear presence of isosbestic points in Figure 4, suggesting a cleanly linear stoichiometric transformation of Ag between the two phases. Nevertheless, for idealized sequential reduction of $\text{Ag}_2\text{VO}_2\text{PO}_4$, 50 and 100% of the Ag species would have been expected to be reduced to metallic Ag at 25 and 50% depths of discharge, which is clearly not the case here. Consequently, LCF of the Ag K-edge data provides further evidence of the concurrent reduction of V^{5+} sites upon the initiation of discharge. At 75% depth of discharge, the vast majority of the accessible Ag atoms have been reduced and there is little change in the relative contributions of the two species upon subsequent complete discharge of the sample. On the basis of the quantification of the Ag species presented in Figure 5A and the vanadium valences determined in Table 1, it is possible to develop reasonable descriptions of the stoichiometries and vanadium oxidation states of the electrochemically lithiated samples. Table 2 summarizes the compositions extracted from a combination of V K- and Ag K-edge XANES data.

An alternative approach has also been used to derive the relative proportions of metallic Ag and $\text{Ag}_2\text{VO}_2\text{PO}_4$ present in the discharged samples using higher energy EXAFS features >50 eV above the absorption edge. Figure 6A shows the Fourier transforms of the k -space data in Figure 5B for the discharged samples with varying extents of lithiation and the $\text{Ag}_2\text{VO}_2\text{PO}_4$ and metallic Ag end members. Qualitatively, it is clear that the envelope of peaks centered around ~ 1.7 \AA in $\text{Ag}_2\text{VO}_2\text{PO}_4$ (correlated to the Ag–O–PO₃ distances on the order of 2.1 \AA indicated in Figure 1B with a phase shift of 0.5 \AA) is diminished with increasing depth of discharge and is replaced by a peak at ~ 2.4 \AA , corresponding to the nearest neighbor distances in fcc Ag. EXAFS modeling of the pseudoradial distribution function has been performed in real space from 1.0–3.8 \AA . A single-component model comprising only parameters for $\text{Ag}_2\text{VO}_2\text{PO}_4$ provides good agreement for the sample with 0% depth of discharge (Figure 6B). In contrast, a two-component model with contributions from both the $\text{Ag}_2\text{VO}_2\text{PO}_4$ and metallic Ag phases has been used to fit the samples with 25 and 50% depths of discharge. Table 3 shows the extracted fitting parameters, which include amplitude factors, x and y , which can be interpreted in terms of the relative contributions from the two end phases to

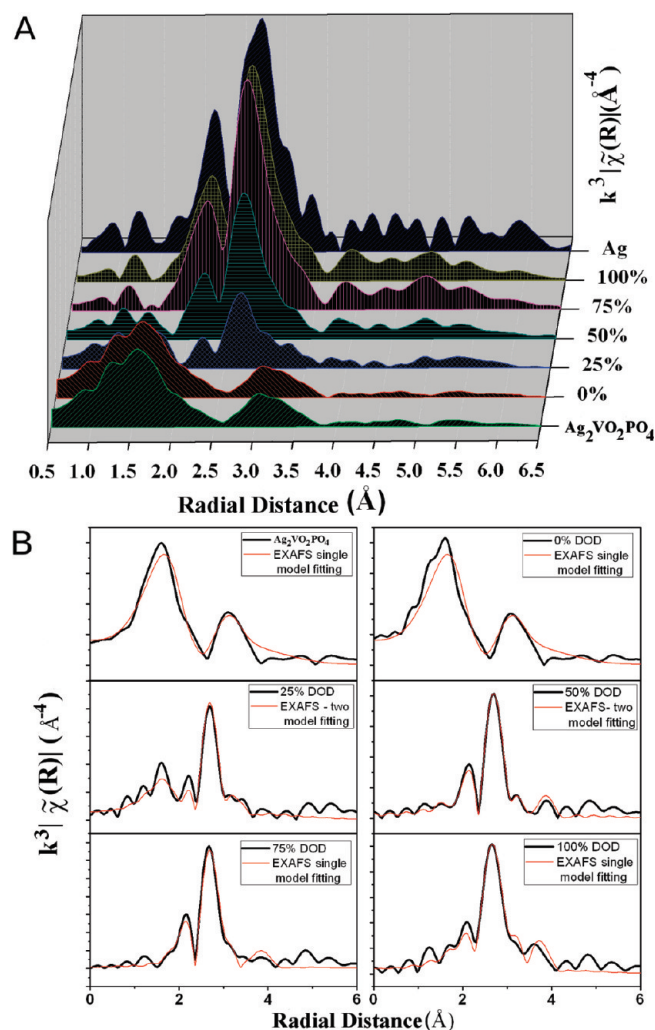


Figure 6. (A) 3D stacked plot of the pseudoradial distribution function in R -space for the end-members $\text{Ag}_2\text{VO}_2\text{PO}_4$ and fcc Ag compared to plots measured for samples at varying depths of discharge. (B) EXAFS modeling using a two-component structure model based on the $\text{Ag}_2\text{VO}_2\text{PO}_4$ and fcc Ag metal end members for samples with varying depths of discharge.

each individual R -space spectrum. As indicated in Figure 6B, a single-component model invoking only the metallic Ag phase is sufficient to fit the Ag K-edge EXAFS data for 75 and 100% depths of discharge suggesting the transformation of a vast majority of the initial Ag^+ ions of $\text{Ag}_2\text{VO}_2\text{PO}_4$ to metallic Ag in these samples. Inclusion of trace $\text{Ag}_2\text{VO}_2\text{PO}_4$ did not substantially improve the obtained fits. The relative proportions of metallic Ag determined from fitting the EXAFS oscillations in R -space (Table 3) are somewhat lower than determined using the LCF fitting of the XANES features. These lower values derived from theoretical models of EXAFS data result from the under-coordination of the absorbing Ag atoms when investigating nanoscale particles such as are constituted from the extruded Ag atoms upon discharge.³⁰ The large contribution from Ag atoms located on the surfaces of the extruded Ag nanoparticles yields an underestimate of the metallic Ag concentration. Table 3 suggests that $23\% \pm 7\%$ and $56\% \pm 6\%$ of total Ag species are present as metallic Ag at 25% and 50% depths of discharge, respectively. The high thermal disorder of Ag (also evidenced in

single crystal structure refinements)¹⁶ within the open layers of the ab plane in the $\text{Ag}_2\text{VO}_2\text{PO}_4$ crystal structure results in a somewhat diffuse average absorber position for Ag atoms in $\text{Ag}_2\text{VO}_2\text{PO}_4$ and is likely responsible for the somewhat higher factors obtained in fitting the $\text{Ag}_2\text{VO}_2\text{PO}_4$ and 0% depth of discharge samples. The relative contributions from Ag and $\text{Ag}_2\text{VO}_2\text{PO}_4$ noted here further confirms the ideas of concurrent, and not sequential, reduction of the two transition metal centers and corroborates that the vast majority of Ag^+ species are reduced to Ag^0 upon electrochemical lithiation to 75% depth of discharge.

V L-Edge. While considerable attention has been devoted to determining the electronic structure of the structurally related vanadyl pyrophosphate $(\text{VO}_2)_2\text{P}_2\text{O}_7$ phases that potentially show Heisenberg spin-1/2 chain behavior,^{24e,g} virtually nothing is known about the band structure of $\text{Ag}_2\text{VO}_2\text{PO}_4$. Figure 7 shows V L- and O K-edge NEXAFS spectra acquired for the $\text{Ag}_2\text{VO}_2\text{PO}_4$ samples that can be understood with reference to the atom- and orbital-projected density of states calculated using DFT and plotted in Figure 8.

The envelopes of peaks labeled V L_{III} - and L_{II} -edges in Figure 7 correspond to transitions from $\text{V } 2p_{3/2}$ and $\text{V } 2p_{1/2}$ core levels, respectively, to V 3d states that are relatively localized or atomic in nature.^{24a,b} The V L_{III} peak is strongly split into two distinctive bands at 516 and 518.3 eV, whereas the V L_{II} feature has two bands at 523.8 and 525.5 eV. The V L_{II} peak is not very informative due to Coster–Kronig Auger decay processes into a $2p_{3/2}$ hole and will not be further discussed.^{24a,31} With increasing extent of discharge, the low-energy 516 eV shoulder of the V L_{III} peak is clearly diminished in intensity relative to the 518.3 eV peak. Since there is only a unique crystallographic position for vanadium in $\text{Ag}_2\text{VO}_2\text{PO}_4$ (Figure 1), the splitting noted here is likely a result of the ligand field splitting of V 3d orbitals under the influence of an approximately octahedral crystal field. The $d_{x^2-y^2}$ and d_{z^2} orbitals (with e_g symmetry) are directed toward the oxide ligands and participate in strong σ interactions with O 2p orbitals, whereas the d_{xz} , d_{xy} , and d_{yz} orbitals (with t_{2g} symmetry) overlap sideways with O 2p levels to form delocalized π -bonding molecular orbitals. The higher energy 518.3 eV band can be assigned to unoccupied states with e_g^* symmetry; the stronger σ interaction stabilizes the bonding levels in the occupied density of states (valence band) and thus destabilizes the antibonding levels in the UDOS (conduction band), shifting the corresponding NEXAFS feature above the t_{2g}^* band at 516 eV. Remarkably, the ligand field splitting of 2.3 eV is verified by the atom-projected density of states plot derived from DFT calculations shown in Figure 8A as the separation between two maxima in the 3d-projected UDOS of $\text{Ag}_2\text{VO}_2\text{PO}_4$. Figure 8B shows the UDOS deconvoluted into specific orbital contributions and clearly indicates that states derived with prominent d_{z^2} and the $d_{x^2-y^2}$ contributions have pronounced maxima that are raised in energy with respect to the overlapping maxima of states derived from d_{xz} , d_{yz} , and d_{xy} orbitals. As has been determined for other vanadium oxide phases,^{24c,d,32} Figure 8A indicates that the occupied levels below the Fermi level primarily have O 2p character, whereas the unoccupied states immediately above the Fermi level are primarily derived from V 3d levels. Despite the excellent agreement between experiment and theory obtained here for the crystal field splitting and the separation of unoccupied states with t_{2g}^* and e_g^* symmetry (Figures 7 and 8), an important caveat is that NEXAFS spectra do not directly mirror the unoccupied density of states

Table 3. EXAFS Fitting Parameters for Each Depth of Discharge Sample^a

DOD	Ag ₂ VO ₂ PO ₄ (x)	E ₀	EXAFS modeling parameters				E ₀	σ^2	ΔR	R-factor
			σ^2	ΔR	Ag (y)					
Ag ₂ VO ₂ PO ₄	0.98 ± 0.12	4.2 ± 1.8	0.02 ± 0.01	0.05 ± 0.03						0.0621
0%	0.93* ± 0.15	4.1 ± 1.3	0.027 ± 0.007	0.083 ± 0.03						0.051
25%	0.77 ± 0.08	3.3 ± 1.1	0.023 ± 0.005	0.03 ± 0.01	0.23 ± 0.08	3.45 ± 0.6	0.012 ± 0.002	0.027 ± 0.011		0.035
50%	0.44 ± 0.07	2.8 ± 1.6	0.011 ± 0.004	0.04 ± 0.02	0.56 ± 0.06	2.07 ± 0.4	0.013 ± 0.003	0.028 ± 0.018		0.031
75%					0.68* ± 0.06	0.9 ± 0.41	0.012 ± 0.003	0.026 ± 0.01		0.024
100%					0.82* ± 0.08	0.4 ± 0.2	0.04 ± 0.008	0.011 ± 0.008		0.015

^a Each parameter was taken directly from the fitting model results in Artemis. X and Y parameter establishes relative percentages for each structural model. E₀ represents a shift on the energy grid for the model. Each σ^2 term addresses thermal disorder while each Δ term models small changes in relevant scattering paths and their corresponding bond lengths.

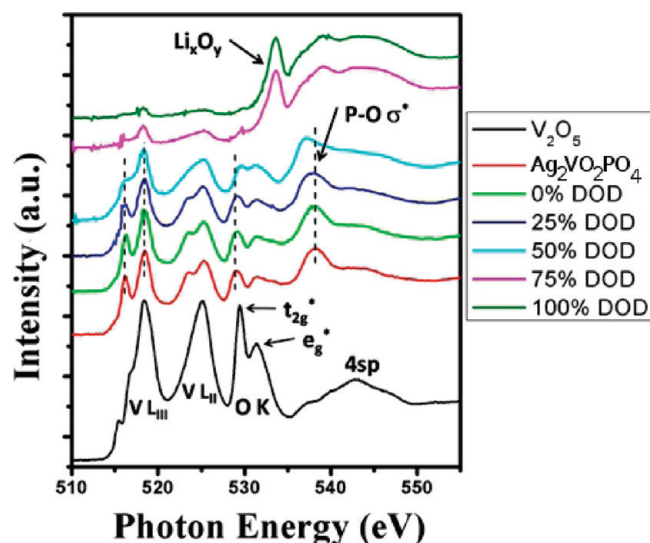


Figure 7. V L-edge and O K-edge NEXAFS spectra for Ag₂VO₂PO₄ and the discharged samples. Data for V₂O₅ standard is also shown for comparison. The resonance assignments are depicted in the figure. The dotted lines serve as visual guides for relative shifting and important points for discussion. Note the strong splitting and subsequent changes to resonances for V-L₃, -L₂, and O-K. At high depths of discharge (75 and 100%), a dramatic change occurs displaying a large resonance near 534 eV along with two broad features from 535 to 550 eV.

owing to the specifics of the transition matrix elements (which can substantially alter the relative peak intensities) and self-energy effects (alteration of the UDOS by the core hole created upon photoexcitation as well as core–hole relaxation effects). Neither of the latter two parameters is expressly addressed in the theoretical calculations presented in Figure 8.

A clear attenuation of the low-energy 516.0 eV t_{2g}^* band at the V L_{III}-edge is evidenced with increasing lithiation of the samples. At 50% depth of discharge, the t_{2g}^* feature is discernibly weaker than the 518.3 eV e_g^* feature and this effect is far more pronounced for the sample with 75% depth of discharge. With increasing reduction of V⁵⁺ down to V³⁺ and V⁴⁺, as also evidenced by V K-edge XANES measurements, the states derived from V 3d levels start to get filled. The transferred electrons reside in the low-energy t_{2g}^* states, thereby reducing the density of holes in these states (as well as altering the V 3d–O 2p hybridization). The increased filling of the lowest available states, which correspond to V 3d- t_{2g}^* overlapped by O 2p is thus

reflected in a diminution of the corresponding NEXAFS feature. This rehybridization and shift in the Fermi level is further verified by the Chaurand plot in Figure 3 depicting substantial changes in the oxidation state and local geometry of vanadium.

O K-Edge. We next turn our attention to the O K-edge spectra depicted in Figure 7. The O K-edge features reflect transitions from O 1s core levels to O 2p states and can be used to sensitively map out features of the UDOS above the Fermi level because of the hybridization of the final states with V 3d levels.^{24b,33} In analogy with the V₂O₅ standard data presented in Figure 7, the observed splitting of the O K-edge feature with distinctive resonances centered around 529.2 and 531.6 eV originates again from the differential hybridization of O 2p levels with different V 3d states.^{24c,33} Vanadium d_{z^2} and $d_{x^2-y^2}$ orbitals are pointed directly at the ligands and thus participate in strong σ interactions characterized by low-lying states in the valence band that in turn are mirrored by high-lying states in the conduction band at 531.6 eV. The Vd_{zx}, d_{zy}, and d_{xy} orbitals participate in relatively weaker π interactions with O 2p orbitals characterized by smaller bonding–antibonding splitting and give rise to the lower energy feature at 529.2 eV. The ~2.4 eV splitting of the O K-edge feature closely matches the value of the ligand field splitting determined at the V L_{III} edge and computed by DFT and can be contrasted to the 2.2 eV crystal field splitting of V₂O₅.^{24b,32} Notably, the ligand field splitting values take into account covalent contributions to V–O bonding that are clearly quite prominent in this system given the strong intensity of the t_{2g}^* and e_g^* peaks relative to the broad feature centered at ~543 eV that can be attributed to transitions to O 2p states hybridized with V 4sp levels.³³ Nevertheless, comparisons of the relative intensities of the t_{2g}^* and e_g^* features to the broad V 4sp resonances for Ag₂VO₂PO₄ and a V₂O₅ standard sample (with an identical oxidation state of +5 for vanadium) suggests substantially reduced covalency for Ag₂VO₂PO₄ relative to the binary vanadium oxide standard. Diminution of transition-metal 3d–O 2p hybridization is known to substantially reduce the intensity of NEXAFS features³³ corresponding to σ and π bonding and hence the observations here corroborate the contention that the incorporation of PO₄³⁻ moieties weakens V–O bonding as a result of the inductive effects of the phosphorus atom.³⁴

The atom-projected UDOS plots in Figure 8A,B verify the hybridization of V 3d and O 2p states and further corroborate the approximately cubic 2.3 eV splitting of states derived from V 3d orbitals of t_{2g}^* and e_g^* symmetry. A well-defined feature at higher energy near 538 eV is most likely derived from strong P–O 2p σ interactions such as will undoubtedly be present for the atom

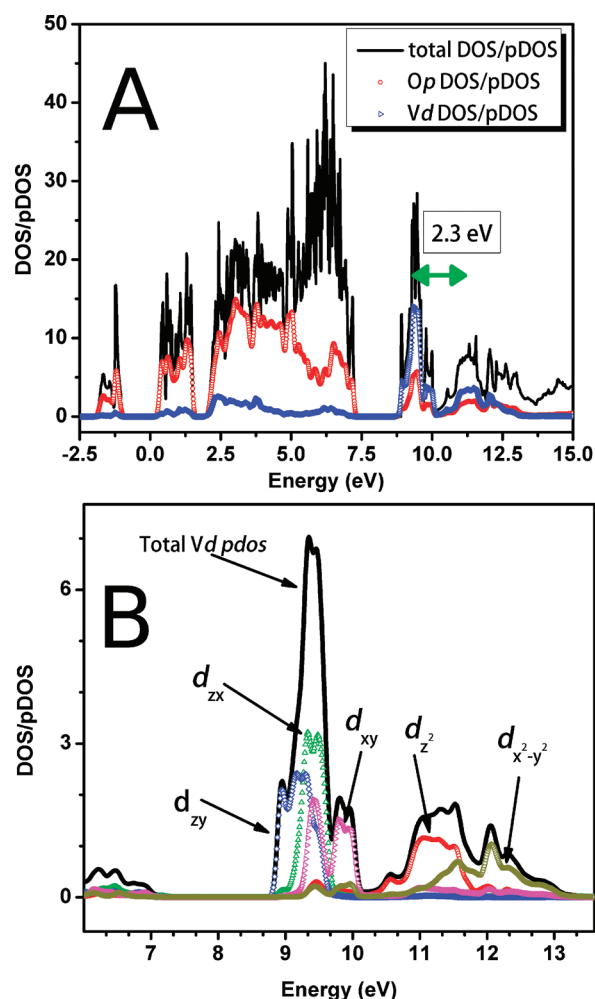


Figure 8. (A) Plot of the total density of states (DOS) for $\text{Ag}_2\text{VO}_2\text{PO}_4$ along with O p-orbital contributions and V d-orbital contributions. O p strongly contributes below the Fermi level in the valence band while V d DOS dominates at the cusp of the conduction band. (B) V d-DOS are resolved to the five contributing d-orbitals with d_{zx} , d_{yz} , and d_{xy} constituting the peaks near 2 eV and the states near 4.5 eV mostly consisting of $d_{x^2-y^2}$ and d_{z^2} . The splitting between these features is consistent with the approximate 2.3 eV splitting observed experimentally in the NEXAFS data.

labeled O(4) in Figure 1B that is not shared with a $[\text{VO}_6]$ octahedron and is directed toward the outside of the vanadyl phosphate layer where it coordinates a Ag^+ ion. It can be seen that this prominent feature is absent in the spectrum for V_2O_5 in Figure 7 and indeed an analogous feature has been observed in O K-edge NEXAFS spectra of $(\text{VO})_2\text{P}_2\text{O}_7$ and $\beta\text{-VOPO}_4$.^{24f,g} The relatively high energy of this feature reflects the strength of the covalent P–O σ bond. Even under conditions of deep discharge, this feature is retained (albeit somewhat shifted), verifying the structural integrity of PO_4^{3-} groups. The shifts to higher energy likely reflect stronger P–O bonding as the coordinated Ag^+ ions are reduced and replaced by more mobile Li^+ species.

With increasing extent of electrochemical lithiation, Figure 7 shows clear evidence of changes in the relative intensities of the NEXAFS features corresponding to t_{2g}^* and e_g^* states. The low-energy resonance is more intense in the parent $\text{Ag}_2\text{VO}_2\text{PO}_4$ material but gradually diminishes in intensity until the two peaks

are approximately of equal intensity in the sample with 50% depth of discharge. Notably, both t_{2g}^* and e_g^* peaks are diminished upon lithiation with respect to the P–O σ^* and V 4sp features. The observed rehybridization can be understood based on filling of the V 3d levels as V^{5+} is reduced to V^{3+} ; since the lower-lying t_{2g}^* orbitals are filled first, the shrinking of the unoccupied levels (reduced density of holes) is reflected in attenuation of the t_{2g}^* peak. In general, as the vanadium atom goes from a d^0 to a d^2 configuration, rehybridization reduces the intensity of both t_{2g}^* and e_g^* resonances relative to the P–O σ^* feature. The subtle shift of the t_{2g}^* feature to higher energy is likely not a reflection of stronger π bonding but instead suggests that the lower-energy maxima in the overlapping t_{2g}^* set are now occupied, thus increasing the spectral weight of the empty higher-lying levels. According to the orbital-projected UDOS shown in Figure 8B, the sequence of V 3d states occupied upon electrochemical reduction from lower to higher energy will follow: V $3d_{zy}$ then $3d_{zx}$, and finally $3d_{xy}$.

At deep (75 and 100%) discharge, a dramatic transformation of the O K-edge is evidenced with the appearance of a prominent resonance at 534 eV. This intense set of peaks is indicative of the formation of Li_xO_y species such as Li_2O and Li_2O_2 .³⁵ In view of the surface sensitivity of NEXAFS detection in PEY mode, the detected species may originate from surface oxidation of the cathode material during cell disassembly and sample preparation. In the absence of in situ experiments, a conclusive determination is not possible. Notwithstanding, the combination of V L-edge and O K-edge measurements and DFT calculations allow for a precise orbital-specific description of vanadium reduction, evidence the role of the PO_4^{3-} group in reducing V–O covalency, and attest to the stability of the phosphate group even under conditions of deep discharge.

CONCLUSIONS

A combination of XANES and EXAFS spectroscopy at various vanadium, oxygen, and silver atomic absorption edges has been used in conjunction with DFT calculations to develop a systematic understanding of the geometric and electronic structure of electrochemically lithiated phases formed by discharging an intriguing $\text{Ag}_2\text{VO}_2\text{PO}_4$ cathode material. Notably, the amorphization of this material upon lithiation precludes full understanding using only conventional powder diffraction methods.

Hard-X-ray V K-edge XANES and Ag K-edge XANES and EXAFS measurements suggest the concurrent and not sequential reduction of the Ag^+ and V^{5+} redox-active sites of $\text{Ag}_2\text{VO}_2\text{PO}_4$, although complete reduction of Ag^+ to nanoparticulate Ag^0 metal precedes the appearance of a significant concentration of V^{3+} species in the discharged phases, which parallels closely with previous studies on the discharge characteristics of the similar silver vanadium oxide system, $\text{Ag}_2\text{V}_4\text{O}_{11}$.^{23b} These measurements further enable a quantitative description of the stoichiometry and redox nature of samples at varying depths of discharge.

Soft X-ray V L- and O K-edge NEXAFS spectroscopy in conjunction with DFT calculations provide the first description of the electronic structure of $\text{Ag}_2\text{VO}_2\text{PO}_4$ and evidence the stability of phosphate groups to advanced states of discharge and reduced covalency of V–O linkages. These specific structural characteristics make this system an attractive cathode material. These measurements further provide an exquisitely detailed picture of orbital occupancies as a function of the depth of

discharge and directly evidence V–O rehybridization accompanying the electrochemical lithiation of $\text{Ag}_2\text{VO}_2\text{PO}_4$. The methodologies developed here are applicable in principle to any cathode material without any crystallinity requirements to obtain a detailed picture of how geometric and electronic structure varies as a function of electrochemical lithiation.

AUTHOR INFORMATION

Corresponding Author

*E-mail: (K.J.T.) takeuchi@buffalo.edu; (E.S.T.) et23@buffalo.edu; (S.B.) sb244@buffalo.edu.

ACKNOWLEDGMENT

S.B. acknowledges partial support of this work from the National Science Foundation under DMR 0847169. S.B. also acknowledges the Donors of the American Chemical Society Petroleum Research Fund for support of this research through 50201DNI10. We acknowledge the computational support provided by the Center for Computational Research at the University at Buffalo, SUNY. P.Z. is supported by the National Science Foundation under Grant DMR-0946404. E.S.T., K.J.T., and A.C.M. acknowledge the U. S. Department of Energy, Division of Materials Science, Grant DE-SC0002460 for support related to the materials synthesis and electrochemical studies. Certain commercial names are presented in this manuscript for purposes of illustration and do not constitute an endorsement by the National Institute of Standards and Technology. The authors would also like to acknowledge K. Tanzil for electrochemical test cell assembly.

REFERENCES

- (1) Van Schalkwijk, W.; Scrosati, B. *Advances in Lithium-Ion Batteries*; Kluwer/Plenum: New York, 2002.
- (2) (a) Whittingham, M. S. *Chem. Rev.* **2004**, *104*, 4271–4301. (b) Winter, M.; Jurgens, O. B.; Spahr, M. E.; Novak, P. *Adv. Mater.* **1998**, *10*, 725–763. (c) Tarascon, J.-M.; Armand, M. *Nature* **2001**, *414*, 359–367. (d) Whittingham, M. S. *Dalton Trans.* **2008**, 5424–5431.
- (3) (a) Takeuchi, E. S.; Leising, R. A. *MRS Bull.* **2002**, *27*, 624–627. (b) Kang, K.-Y.; Meng, Y. S.; Breger, J.; Grey, C. P.; Ceder, G. *Science* **2006**, *311*, 977–980. (c) Chung, S.-Y.; Bloking, J. T.; Chiang, Y.-M. *Nat. Mater.* **2002**, *1*, 123–128.
- (4) (a) Kang, B.; Ceder, G. *Nature* **2009**, *458*, 190–193. (b) Arico, A. S.; Bruce, P.; Scrosati, B.; Tarascon, J.-M.; van Schalkwijk, W. *Nat. Mater.* **2005**, *4*, 366–377. (c) Hirshes, M. *Mater. Sci. Eng., B* **2004**, *108*, 1–15. (d) Nazar, L.; Goward, G.; Leroux, F.; Duncan, M.; Huang, H.; Kerr, T.; Gaubicher, J. *Int. J. Inorg. Mater.* **2001**, *3*, 191–200.
- (5) Albrecht, T. A.; Sauvage, F.; Bodenez, V.; Tarascon, J.-M.; Poeppelmeier, K. R. *Chem. Mater.* **2009**, *21*, 3017–3020.
- (6) Takeuchi, E. S.; Takeuchi, K. J.; Marschilok, A. C.; Suny, B. *Lithium – Vanadium/Silver Oxides*; Elsevier B.V.: New York, 2009.
- (7) (a) Takeuchi, K. *Coord. Chem. Rev.* **2001**, *219–221*, 283–310. (b) Tracey, A. S.; Willsky, G. R.; Eds., *Vanadium: Chemistry, Biochemistry Pharmacology and Practical Applications*; CRC Press: Boca Raton, FL, 2007; p 200.
- (8) Leising, R. A.; Thiebolt, W. C.; Takeuchi, E. S. *Inorg. Chem.* **1994**, *33* (25), 5733–5740.
- (9) Tarascon, J. M.; Delacourt, C.; Prakash, A. S.; Morcrette, M.; Hegde, M. S.; Wurm, C.; Masquelier, C. *Dalton Trans.* **2004**, No. 19, 2988–94.
- (10) (a) Morcrette, M.; Martin, P.; Rozier, P.; Vezin, H.; Chevallier, F.; Laffont, L.; Poizot, P.; Tarascon, J.-M. *Chem. Mater.* **2005**, *17*, 418–426. (b) Morcrette, M.; Rozier, P.; Dupont, L.; Mugnier, E.; Sannier, L.; Galy, J.; Tarascon, J.-M. *Nat. Mater.* **2003**, *2*, 755–761.
- (11) Padhi, A. K.; Nanjundaswamy, K. S.; Goodenough, J. B. *J. Electrochem. Soc.* **1997**, *144*, 1188–1194.
- (12) (a) Marschilok, A. C.; Takeuchi, K. J.; Takeuchi, E. S. *Electrochem. Solid-State Lett.* **2009**, *12*, A5–A9. (b) Takeuchi, E. S.; Marschilok, A. C.; Tanzil, K.; Kozarsky, R. S.; Zhu, S.; Takeuchi, K. J. *Chem. Mater.* **2009**, *21*, 4934–4939.
- (13) Kim, Y. J.; Marschilok, A. C.; Takeuchi, K. J.; Takeuchi, E. S. *J. Power Sources* **2011** in press.
- (14) Marschilok, A. C.; Kozarsky, E. S.; Tanzil, K.; Zhu, S.; Takeuchi, K. J.; Takeuchi, E. S. *J. Power Sources* **2010**, *195* (19), 6839–6846.
- (15) Teo, B. K. *EXAFS: Basic Principal and Data Analysis Inorganic Chemistry Concepts*; Springer: Heidelberg, Germany, 1986; Vol. 9.
- (16) Kang, H.-Y.; Wang, S.-L.; Tsai, P.-P.; Lü, K.-H. *J. Chem. Soc., Dalton Trans.* **1993**, 1525–1528.
- (17) Ravel, B.; Newville, M. *J. Synchrotron Radiat.* **2005**, *12*, 537–541.
- (18) Ravel, B.; Newville, M. *Phys. Scr.* **2005**, *T115*, 1007–1010.
- (19) Giannozzi, P.; Baroni, S.; Bonini, N.; et al. *J. Phys.: Condens. Matter* **2009**, *21*, 395502/1–19.
- (20) Perdew, J.; Burke, K.; Ernzerhof, M. *Phys. Rev. Lett.* **1996**, *77* (18), 3865–3868.
- (21) Vanderbilt, D. *Phys. Rev. B* **1990**, *41* (11), 7892–7895.
- (22) (a) Koningsberger, D. C.; Prins, R. *X-ray Absorption: Principles, Applications, Techniques of EXAFS, SEXAFS, and XANES*; John Wiley: New York, 1988. (b) Stohr, J. *NEXAFS Spectroscopy*; Springer: Berlin, 1992; (c) Chen, J. G. *Surf. Sci. Rep.* **1997**, *30*, 1–152.
- (23) (a) Stallworth, P. E.; Kostov, S.; denBoer, M. L.; Greenbaum, S. G.; Lampe-Onnerud, C. *J. Appl. Phys.* **1998**, *83*, 1247–1255. (b) Leifer, N. D.; Colon, A.; Martocci, K.; Greenbaum, S. G.; Alamgir, F. M.; Reddy, T. B.; Gleason, N. R.; Leising, R. A.; Takeuchi, E. S. *J. Electrochem. Soc.* **2007**, *154*, A500–A506.
- (24) (a) Goering, E.; Muller, O.; Klemm, M.; denBoer, M. L.; Horn, S. *Philos. Mag. B* **1997**, *75*, 229–236. (b) Eyert, V.; Hock, K.-H. *Phys. Rev. B* **1998**, *57*, 12727–12736. (c) Velazquez, J. M.; Jaye, C.; Fischer, D. A.; Banerjee, S. J. *Phys. Chem. C* **2009**, *113*, 7639–7645. (d) Abbate, M.; De Groot, F. M. F.; Fuggle, J. C.; Ma, Y. J.; T., C. C.; Sette, F.; Fujimori, A.; Ueda, Y.; Kosuge, K. *Phys. Rev. B* **1991**, *43*, 7263–7266. (e) Havecker, M.; Knop-Gericke, A.; Mayer, R. W.; Fait, M.; Bluhm, H.; Schlögl, R. *J. Electron. Spectrosc. Relatd. Phenom.* **2002**, *125*, 79–87. (f) Willinger, M. G.; Su, D. S.; Schlögl, R. *Phys. Rev. B* **2005**, *155*118/1–155118/8. (g) Gerhold, S.; Nucker, N.; Kuntscher, C. A.; Schuppler, S.; Stadler, S.; Idzerda, Y. U.; Prokofiev, A. V.; Bullesfeld, F.; Assmus, W. *Phys. Rev. B* **2001**, *63*, 073103/1–073103/4.
- (25) Yamamoto, T. *X-ray Spectrometry* **2008**, *37*, 572–584.
- (26) Wong, J.; Lytle, F. W.; Messmer, R. P.; Maylotte, D. H. *Phys. Rev. B* **1984**, *30*, 5596–5610.
- (27) Sipr, O.; Simunek, A.; Bocharov, S.; Kirchner, T.; Drager, G. *Phys. Rev. B* **1999**, *60*, 14115–14227.
- (28) Chaurand, P.; Rose, J.; Briois, V.; Salome, M.; Proux, O.; Nassif, V.; Olivi, L.; Susini, J.; Hazemann, J.-L.; Bottero, J.-Y. *J. Phys. Chem. B* **2007**, *111*, 5101–5110.
- (29) Whittaker, L.; Velazquez, J. M.; Banerjee, S. *CrystEngComm* **2010**10.1039/c0ce00832j.
- (30) (a) Glasner, D.; Frenkel, A. I. *AIP Conf. Proc.* **2007**, *882*, 746–748. (b) Beale, A. M.; Weckhuysen, B. M. *Phys. Chem. Chem. Phys.* **2010**, *12* (21), 5562–5574. (c) Jentys, A. *Phys. Chem. Chem. Phys.* **1999**, *1* (17), 4059–4063.
- (31) Zaanen, J.; Sawatzky, G. A. *Phys. Rev. B* **1986**, *33*, 8074–8083.
- (32) (a) Kolczewski, C.; Hermann, K. *Surf. Sci.* **2004**, *552*, 98–110. (b) Kolczewski, C.; Hermann, K. *Phys. Scr.* **2005**, *T115*, 128–130.
- (33) deGroot, F. M. F. G.; Fuggle, J. C.; Ghijsen, J.; Sawatzky, G. A.; Peterson, H. *Phys. Rev. B* **1989**, *40*, 5715–5723.
- (34) Padhi, A. K.; Nanjundaswamy, K. S.; Goodenough, J. B. *J. Electrochem. Soc.* **1997**, *144* (4), 1188–1194.
- (35) Deng, D.; Kim, M. G.; Lee, J. Y.; Cho, J. *Energy Environ. Sci.* **2009**, *2*, 818–837.